Numerical Investigation of a Transformable Modular PET System: Consideration of Point-Spread Functions, Module Arrangements, and Operation Protocols

Yu-Fen Chang[1,3,a)], Kyle Thompson[1], Aram Teymurazyan[1], Steven D. Siciliano[2] and Zisis Papandreou[1]

[1]*Department of Physics, University of Regina, 3737 Wascana Parkway, Regina, Saskatchewan S4S 0A2, Canada*
[2]*Department of Soil Science, University of Saskatchewan, 51 Campus Drive, Saskatoon S7N 5A8, Canada*
[3]*Department of Physics and Technology, University of Bergen, Allégaten 55, 5007 Bergen, Norway*

[a)]Corresponding author: Yu-Fen.Chang@uregina.ca, Yu-Fen.Chang@uib.no

Abstract. Positron emission tomography (PET) is a powerful tool for mapping the dynamic distribution of substances in visually opaque systems. A modular, scalable, transformable, and relocatable PET system is custom built to provide optimized flexible PET imaging for a wider variety of applications. In coordination with the purposely designed hardware, we develop adaptive data processing and image reconstruction pipelines. We perform Monte Carlo simulation and demonstrate the application of the developed pipelines to investigate the impacts of varied point-spread functions (PSFs), module arrangements, and PET operation protocols on image quality. This study manifests the consequences of employing unoptimized PSFs and the necessity of implementing space-variant and anisotropic PSFs for optimizing the resolution across the FOV for different module arrangements and operational conditions.

INTRODUCTION

Modular positron emission tomography (PET) systems, being scalable, relocatable, and rearrangeable, are more adaptable to changing objects, conditions, and resolution requirements compared to fixed-geometry PET systems. By incorporating rotation and translation mechanisms, limited number of modules would also be able to cover wider sampling angles and field of views (FOVs) with lower capital cost. A modular PET system, BioPET[1] [2], has been built to provide optimized flexible PET imaging for a wider variety of applications. To achieve this aim, flexible and reliable image reconstruction methods need to be developed in coordination with the purposely designed hardware.

Iterative reconstructions of PET can benefit from using a system matrix, which is a model relating the recorded data to the imaged object by incorporating all the resolution-degrading effects. Reconstructions that employ the image-based point-spread functions (PSFs) to model the system matrix and use the method of sieves [3] can produce artifact-free images with a better compromise between noise and spatial resolution than images reconstructed without or with unoptimized PSFs [4]. However, the use of PSFs can also potentially induce, among others, slower convergence, less reproducible recovery coefficients (RCs), and fluctuated behavior of RCs as a function of object diameter [5]. These drawbacks have highlighted the necessity of optimizing PSF reconstruction for specific systems and tasks.

Monte Carlo (MC) simulation, a method that uses random sampling techniques to arrive at a solution, has been effectively applied to the assessment and optimization of nuclear imaging, including detector and system design as well as reconstruction and correction techniques (see, e.g., [6]). In this work, we develop the image reconstruction pipelines for the modular PET system and apply the pipelines to investigate the influence of PSF reconstructions, PET operation protocols, and module arrangements on the image formation by utilizing MC simulation.

[1]The essential parts of the system were built in collaboration with Thomas Jefferson National Accelerator Facility (JLab) according to custom specifications. Further modifications and expansion were carried out in-house. For detailed information and characterization of the electronics and the data acquisition architecture, refer to [1, 2].

METHODS AND MATERIALS

Simulation Setup

PET data of a phantom imaged by different arrangements of modules operated in static and rotational modes were simulated using an MC modeling package—"Geant4 Application for Tomographic Emission" (GATE) [7]. GATE is an extension of Geant4, which is a particle tracking and transport simulation framework [8].

The phantom is composed of six sections of radioactive rods 3 mm in length and 0.5–1.5 mm in diameter, as shown in Fig. 1 (a). The pattern was adapted from the Anger pie phantom [9]. For each section, the center-to-center distance is quadruple of the diameter.

Three simulation scenarios are presented here. (i) Four modules were respectively placed on each side of a rectangle, facing the FOV. (ii) The arrangement of (i) was rotated about the central axis 30° at a user-defined frequency (Fig. 1 (b)). (iii) Twelve modules were respectively placed on each side of a dodecagon, facing the FOV (Fig. 1 (c)). In all cases, the distance between the opposing detection faces was 182 mm.

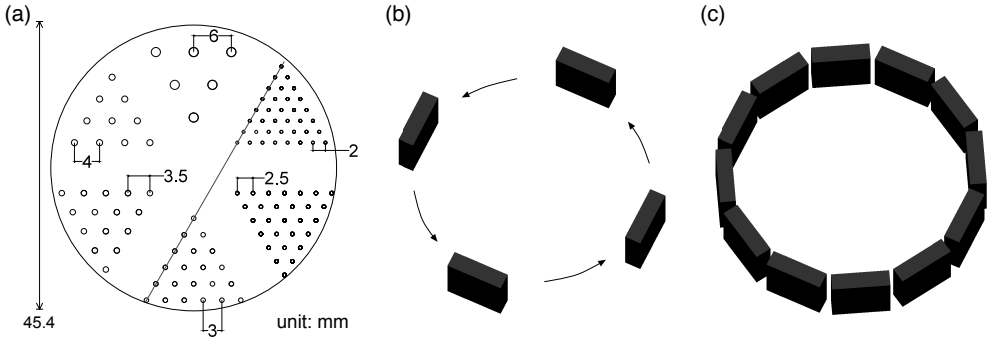

FIGURE 1. The phantom (a) in the FOV center of arrangements of (b) (operated in both static and rotational modes) and (c) (in static mode) were simulated. The phantom was composed of six sections of radioactive rods 3 mm in length and 0.5–1.5 mm in diameter. In each section of the phantom, the center-to-center distance is quadruple of the diameter. A line is drawn through the rods with diameters of 0.75 mm and 0.5 mm for subsequent discussion in this paper. The distance between the opposing detector faces was 182 mm in all detector arrangements as illustrated in (b) and (c).

Each simulated detector module consists of 35 × 35 LYSO:Ce scintillator crystals ($Lu_{1.9}Y_{0.1}SiO_5$) with dimensions of 1.2 × 1.2 × 13 mm^3. A 0.1 mm gap divides the adjacent crystals, resulting in a detection area of 45.4 × 45.4 mm^2 for each module [2].

Photoelectric effect and Compton scatter were modeled using the standard electromagnetic package of Geant4, and Rayleigh scattering was simulated using the PENELOPE model [10]. Gamma non-collinearity and positron range were not simulated. The energy resolution of the detectors was set to 20%, and the coincidence time window was 12 ns. A -20% to +60% energy window was applied around the 511 keV peak.

Image Reconstruction

Data processing pipelines for image reconstruction of the modular PET system were developed and implemented in Fortran and C++, making use of an open-source generic platform—"Customizable and Advanced Software for Tomographic Reconstruction" (CASToR) [11]. The data output from the GATE simulations, consisting of time and crystal identifications, were saved in ROOT format [12], which was then processed into list-mode data. The projector described by Joseph [13] was used. Image-based PSF with the method of sieves was applied to perform i) standard PSF reconstruction, where a convolution of the current estimate is forward-projected and a convolution of the correction terms is used for the update, and ii) post-processing after the termination of iterations by using the PSF as the convolution kernel. The image-based PSF was modeled by a 3D space-invariant and isotropic Gaussian. The images were reconstructed in 161 × 161 × 17 voxels of 0.3 × 0.3 × 0.3 mm^3.

[2]The actual module consists of 37 × 37 crystals and the signals from the two crystals at the array edge are merged, which results in a 35 × 35 crystal map.

To investigate the impact of varied PSF FWHM (full width at half maximum), data acquired in the aforementioned scenario (ii), where four modules were operated in rotational mode, were reconstructed using ordered subset expectation maximization (OSEM) algorithm [14] with 2 iterations and 16 subsets, and with PSFs of 0.2, 0.4, 0.6, 0.8, and 1.0 mm FWHM. The optimal PSF FWHM was then approximated and used in the image reconstruction for scenarios (i) and (iii). 17 million unscattered coincidences (trues + randoms) were used for every reconstruction.

RESULTS AND DISCUSSION

As the image reconstructions incorporating various PSF FWHM for the data of scenario (ii) were carried out, the reconstructed images of central 1.5 mm length of the rods were averaged to obtain a single image slice of lower noise. The min–max pixel values of each averaged image were then linearly scaled to 0–1. Figure 2 shows the profiles of the line, as indicated in Fig. 1 (a), drawn on the averaged images. Artifacts can be seen on the line profile of "PSF FWHM = 0.2 mm," while the line profile of "PSF FWHM = 0.4 mm" displays the peaks distinctly without visible artifacts and without much degradation of signal-to-noise ratios (SNRs) compared to "PSF FWHM = 0.2 mm." However, as the PSF FWHM further increases, the SNRs deteriorate noticeably. The line profile of "PSF FWHM = 0.8 mm" (not shown) presents the in-between state between PSF FWHM = 0.6 and 1.0 mm. The optimal size of PSF FWHM can be approximated as 0.4 mm through the analysis of the trade-off between noise, contrast recovery, and artifact amplitude.

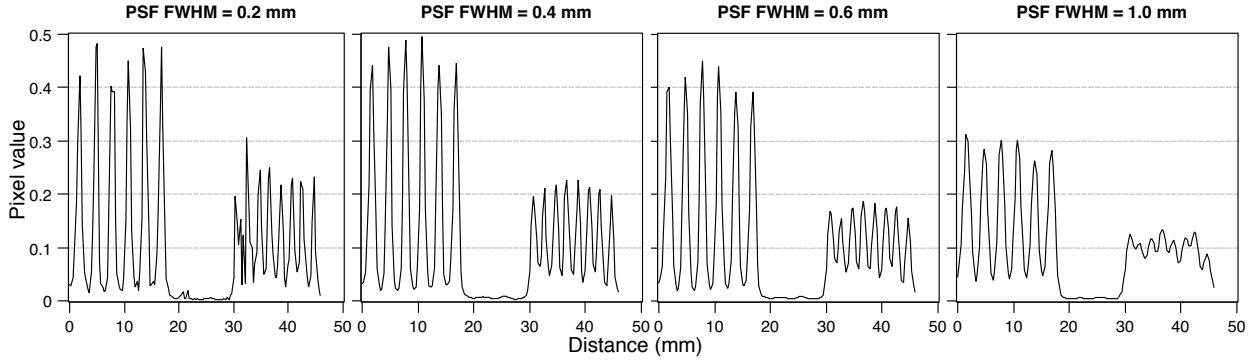

FIGURE 2. Profiles of the line, as indicated in Fig. 1 (a), drawn on the averages of the images of the central 1.5 mm rod reconstructed with PSF FWHM = 0.2, 0.4, 0.6, and 1.0 mm.

The same reconstruction settings, PSF FWHM = 0.4 mm, and image averaging were employed to process the simulated data of scenarios (i) and (iii). Figure 3 (a), (b), and (c) show the averages of the central 1.5 mm rod images reconstructed in scenarios (i), (ii), and (iii), respectively. Under the present simulation settings, the randoms rates of arrangements of four modules (in both static and rotational modes) and twelve modules are 8% and 25%, respectively. The line profiles, as indicated in Fig. 1 (a), of images in Fig. 3 are shown in Fig. 4. As can be computed from the profiles, for the rods closer to the FOV center, the SNRs of the "twelve modules in static mode" and "four modules in rotational mode" are close in quantity. However, in the areas close to the FOV edge the "four modules in rotational mode" produce higher SNRs.

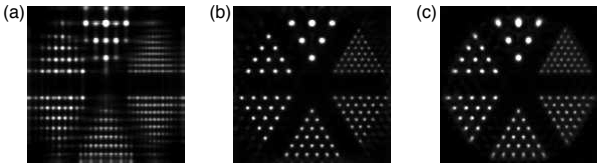

FIGURE 3. (a), (b), and (c) show the reconstructed images of three simulated scenarios, respectively: (i) Static four modules. (ii) The arrangement of (i) was rotated about the central axis 30° at a user-defined frequency. (iii) Static twelve modules. The average images of the central 1.5 mm length of rods are shown here. Image contrast was adjusted by using histogram stretching with identical saturation setting.

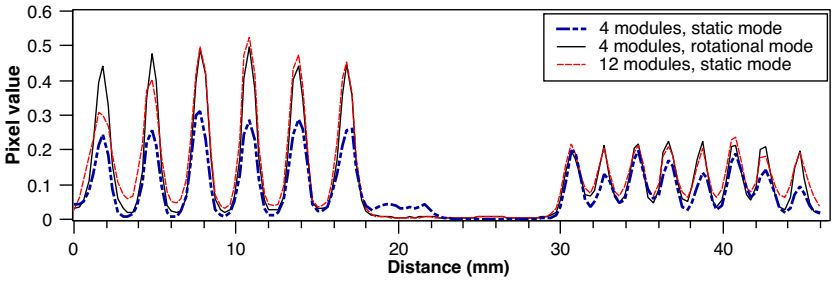

FIGURE 4. Profiles of the lines, as indicated in Fig. 1 (a), drawn on the images in Fig. 3.

CONCLUSION

In this work, we developed data processing pipelines for the modular PET system. We investigated the impacts of varied PSF FWHM, module arrangements, and PET operation protocols on the image quality by utilizing the developed pipelines and Monte Carlo simulation. Results show that unoptimized PSFs cause artifacts and degradation of SNRs. Employing an optimal PSF can achieve better compromise between noise, contrast recovery, and artifact amplitude. The use of four modules and rotation to cover a full ring takes five times longer to acquire the same amount of data but gives higher SNRs over all FOV in the central axial plane compared to a static full ring formed by twelve modules. Further studies are intended to implement space-variant and anisotropic PSFs to further optimize the resolution across the FOV for different module arrangements and operation modes.

ACKNOWLEDGMENTS

This work was partly supported by the Fedoruk Centre with funding from Innovation Saskatchewan and by the project "Designing Crops for Global Food Security" funded by the Canada First Research Excellence Fund.

REFERENCES

[1] A. G. Weisenberger, H. Dong, B. Kross, *et al.*, "Development of PhytoPET: A plant imaging PET system," in *2011 IEEE Nuclear Science Symposium Conference Record* (2011), pp. 275–278.
[2] A. Talebitaher, Y.-F. Chang, K. Thompson, *et al.*, "BioPET: Dedicated plant and soil microorganism positron emission tomography system," in *Proceedings of 38th Annual Conference of the Canadian Nuclear Society* (2018).
[3] U. Grenander, *Abstract Inference* (John Wiley & Sons, 1981).
[4] S. Stute and C. Comtat, Physics in Medicine & Biology **58**, 3849–3870 (2013).
[5] O. L. Munk, L. P. Tolbod, S. B. Hansen, and T. V. Bogsrud, EJNMMI Physics **4**, 5–16 (2017).
[6] I. Buvat, I. Castiglioni, J. Feuardent, and M.-C. Gilardi, Physics in Medicine & Biology **50**, p. 329 (2005).
[7] G. Santin, S. Staelens, R. Taschereau, P. Descourt, C. R. Schmidtlein, L. Simon, D. Visvikis, S. Jan, and I. Buvat, *Proceedings of the 10th Topical Seminar on Innovative Particle and Radiation Detectors*, Nuclear Physics B - Proceedings Supplements **172**, 101–103 (2007).
[8] J. Allison, K. Amako, J. Apostolakis, *et al.*, Nuclear Instruments and Methods in Physics Research Section A: Accelerators, Spectrometers, Detectors and Associated Equipment **835**, 186–225 (2016).
[9] H. Anger, "Testing the performance of scintillation cameras," Tech. Rep. (1973).
[10] J. Baró, J. Sempau, J. M. Fernández-Varea, and F. Salvat, Nuclear Instruments and Methods in Physics Research Section B: Beam Interactions with Materials and Atoms **100**, 31–46 (1995).
[11] T. Merlin, S. Stute, D. Benoit, J. Bert, T. Carlier, C. Comtat, F. Lamare, and D. Visvikis, "CASToR: A generic data organization and processing code framework for multi-modal and multi-dimensional tomographic reconstruction," Poster (IEEE Medical Imaging Conference, 2016).
[12] R. Brun and F. Rademakers, Nuclear Instruments and Methods in Physics Research Section A: Accelerators, Spectrometers, Detectors and Associated Equipment **389**, 81–86 (1997).
[13] P. M. Joseph, IEEE Transactions on Medical Imaging **1**, 192–196 (1982).
[14] H. M. Hudson and R. S. Larkin, IEEE Transactions on Medical Imaging **13**, 601–609 (1994).